Cloud Condensation Model from Radiosonde and Ceilometer Measurements Comparison

Rani Arielly, Adva Baratz, Ran Aharoni and Ofir Shoshanim

Israel Institute for Biological Research, Ness-Ziona 7410001, Israel

Corresponding author: Rani Arielly (rani.arielly@gmail.com)

Key Points:

- Combining radiosonde and ceilometer atmospheric sensing allows testing of novel cloud physics model.
- An initial rate limiting condensation step may be crucial in activating cloud condensation nuclei.
- The smallest effective cloud condensation nucleus size is evaluated.

Abstract

Due to their importance for Earth's climate, the formation of clouds is extensively studied, and especially their formation inside the atmospheric boundary layer (ABL). Radiosonde is one of the most used tools for atmospheric research and studying the ABL in particular, since it is a simple and direct means of measuring a variety of variables. This, however, come at the account of the data not being temporally or laterally focused. Remote sensing methods, such as the light detection and ranging (LiDAR) technique, do not share the radiosonde shortcomings, but on the other hand, produce data that is interpretable. Despite these limitations, using data from both types of systems may provide additional insight. In this work, simultaneous measurements of radiosondes and ceilometer data acquired during a week at the end of November are comparatively analyzed and temporally adjusted. A transformation of the radiosonde's temperature and humidity data into simulated optical backscatter signal is implemented using a condensation model which includes an initial rate limiting step which may be crucial in activating cloud condensation nuclei. Comparing these transformed signals to the ceilometer's measured signals allows studying condensation processes and deducing the size of the smallest effective cloud condensation nucleus.

1 Introduction

Tropospheric clouds are of great importance for Earth's climate. They laterally disperse moisture, and alter the radiative forcing and thus change the planet's heat balance.(Ahrens & Henson, 2019b; Cess et al., 2001) Therefore, the formation of clouds is extensively studied, and especially their formation inside the atmospheric boundary layer (ABL) since this layer is directly influenced by the surface's forcings which include evaporation and transpiration,(Koren et al., 2004; Paluch & Lenschow, 1991; Zhong & Doran, 1997) and due to local pressure gradients that prevent matter from ascending above them.(Stull, 1988a) Due to high activation energies for vapor condensation, one of the most important factors influencing clouds formation is the availability of effective cloud condensation nuclei (CCN), which play an essential role in reducing these phase transitions energies.(Levi & Rosenfeld, 1996) These CCNs may be ice, salt, dust or pollutants for example, and may vary between geographical locations and altitudes.(Andreae et al., 1986) Cloud formation in Israel is heavily infuenced by its most important aerosol source - the large desert area that extends from the Sahara to the southwest, through Sinai and the Negev to the south and the Arabian desert to the east, which provide dust particles transported regularly by winds from as far as 2000 km.(Gagin, 1965; Ganor, 1975; Ganor & Foner, 1996; Ganor & Mamane, 1982; Levi & Rosenfeld, 1996; Levin et al., 1996; Rosenfeld & Farbstein, 1992; Yaalon & Ganor, 1973) These dust particles are mainly composed of Illite and Kaolinite crystals that are poorly hygroscopic but may be coated with solubale materials, depending on the trajectory of the dust.(Attwood & Greenslade, 2011; Chester, 1990; Falkovich et al., 2001; Ganor, 1991; Ghadiri et al., 2015; Levin et al., 1990; Wurzler et al., 2000) The availability and types of CCNs will influence the success in forming a cloud and the resulting droplet size spectra. Several attempts have been made to analytically describe measured particle size distributions with simple mathematical expressions.(Measures, 1992; Takeuchi, 2005) One of these expressions is the log-normal distribution, in which the size distribution is described by a normal distribution with the particle sizes inserted into the Gaussian in a logarithmic scale. This distribution normalized to the total particle number, n_{total}, is

$$n(r_d) = \frac{n_{total}}{r_d\sqrt{2\pi}\sigma_d}\exp\left(-\frac{\left(\ln\frac{r_d}{\bar{r}_d}\right)^2}{2\sigma_d^2}\right) \quad (1)$$

where r_d is the particle radius, $\bar{r}_d$ is the distribution median, and σ_d is the distribution width.

The study of the ABL is one of the most studied fields in atmospheric research.(Jenkin & Clemitshaw, 2000; Nolan et al., 2009; Quan et al., 2013) One of the most used tools in studying the ABL is the radiosonde, which can locally measure many parameters. The common practice in places that require atmospheric data for routine operation is to float radiosondes every couple of hours, relying on that no sharp changes would occur between their flight times, and that the lateral position of the radiosonde at a certain moment would fit the position to which the data is required. These assumptions are not fulfilled in many cases where data that was required for one geographic location at certain altitude and time was actually measured many kilometers away and hours apart.(McGrath et al., 2006; Seidel et al., 2011) Due to these radiosonde measurements shortcomings, additional measurement methods are used. These include local means such as masts that can support a large variety of measurement devices at a specific location, and electromagnetic or supersonic remote sensing methods that can provide a very specific type of data at multiple locations in a very short time. Each of these methods, however, is also limited due to limited measurement altitudes, non-continuous data(Brümmer et al., 2012), inability to change lateral position(Stull, 1988b), or unwanted contributions from regions outside the region of interest(Golbon-Haghighi et al., 2016; A. Rogers et al., 2007), which will determine the measurement representativeness.(Banakh et al., 1995, 2010; Eckstein et al., 2017; Haszpra, 1999; Henne et al., 2010; Kitchen, 1989; Nappo et al., 1982; Piersanti et al., 2015; Schwarz et al., 2017)

LiDAR (Light Detection and Ranging) is a remote sensing device based on electromagnetic interaction with matter in the ultraviolet to infrared regions of the spectrum. Knowing the scattering mechanism, analyzing the LiDAR's signal allows retrieving properties of a scattering medium. The LiDAR device contains a pulsed LASER that emits pulses that progress through space while being absorbed or scattered in some probability by the local medium.(Weitkamp, 2005) Optical scattering from particles with typical size comparable to the wavelength (like some aerosols in the ABL which are sized in the $\sim 0.1-10\ \mu m$ range (Mahowald et al., 2014)) is described by the Mie model.(Bohren & Huffman, 1983a) This model predicts the probability for scattering the radiation at some angle relative to its original direction, which varies according to the particle size to wavelength ratio, and the optical refractive index of the scattering medium. Radiation scattered towards the LiDAR's detector is absorbed, producing an electric signal that is registered as a function of time (t) since the production of the LASER pulse. For back-scattered radiation, the range is $z = \frac{1}{2}ct$, and this signal is (Mattis & Wagner, 2014)

$$P(z) = C\ O(z)\alpha(z)S^{-1}(z)/z^2 e^{-2\int_0^z \alpha(z')dz'} \quad (2)$$

where $P(z)$ is the raw detector signal (from which the dark current and atmospheric background signals are subtracted), $O(z)$ is the laser and detector fields of view overlap function, C is a variable that incorporates various characteristic of the system such as the intensity and temporal-width of the laser pulse, the area of the detector, and the quantum efficiency of the detector, $S(z)$ is the LiDAR ratio, and $\alpha(z)$ is the volume extinction coefficient. Cilometer is a LiDAR device for

atmospheric uses. It is primarily used for determining the cloud base height, it's thickness, and the cloud cover for airports, but can also be used for measuring aerosol concentrations and visibility. Each pulse of the ceilometer's LASER provides a vertical two-way attenuated optical backscatter profile, $B(z) = \frac{P(z)z^2}{C\ O(z)}$. (Vaisala, 2017b, 2017a)

All above mentioned measurement devices have their limitations, thus sometimes it is preferable to use multiple devices simultaneously in order to verify results. However, when considering the technical basis by which these devices perform, it may become apparent that using data from multiple types of devices may provide additional insight. In this work we comparatively analyze and temporally adjust data from simultaneous measurements of radiosondes and ceilometer acquired during a week at the end of November. A transformation of the radiosonde's temperature and humidity data into simulated optical backscatter signal is proposed and implemented. Comparing these transformed signals to the ceilometer's measured signals allows studying condensation processes and deducing the size of the smallest effective cloud condensation nucleus.

2 Measurements

Atmospheric data was collected by floating ten Meteomodem M10 radiosondes, over a week at the end of November in the morning, noon, evening and night.(Arielly, 2020) The M10 device simultaneously measured lateral location, altitude, horizontal and vertical velocities of the device, Pressure, temperature, relative humidity, and the wind's speed and direction, and transmitted them by radio broadcast to the SR10 receiver device (maximum transmission distance about 350 km). The M10 has a maximum reliable work height of about 30 km. The radiosondes' flight data including the radiosonde number, its flight time and maximum height arrival time are shown in **Table 1**, and their trajectories including horizontal position and elevation (indicated by the color of the trajectory) are shown in **Figure 1** on top of satellite images. Measurements were also acquired with Vaisala's CL51 ceilometer system at the same time as the radiosonde data measurements.(Arielly, 2020) The ceilometer includes a LASER source that emits $910(10)\ nm$ radiation in $\sim 110\ nsec$ pulses. This radiation is back-scattered by the medium in which it moves and absorbed at the detector component which collects 1540 samples in units of $(10^5 \cdot srad\ \cdot km)^{-1}$ at a rate of 15 MHz which amounts to a spatial resolution of 10 meters and a maximum range of 15.4 km. The ceilometer produces radiation pulses at a 6500 Hz repetition rate and sum the detector data at each range memory bin for 5 seconds to improve the signal to noise ratio. This process is repeated every 36 seconds and produces a new measurement of two-way attenuated optical backscatter profile.

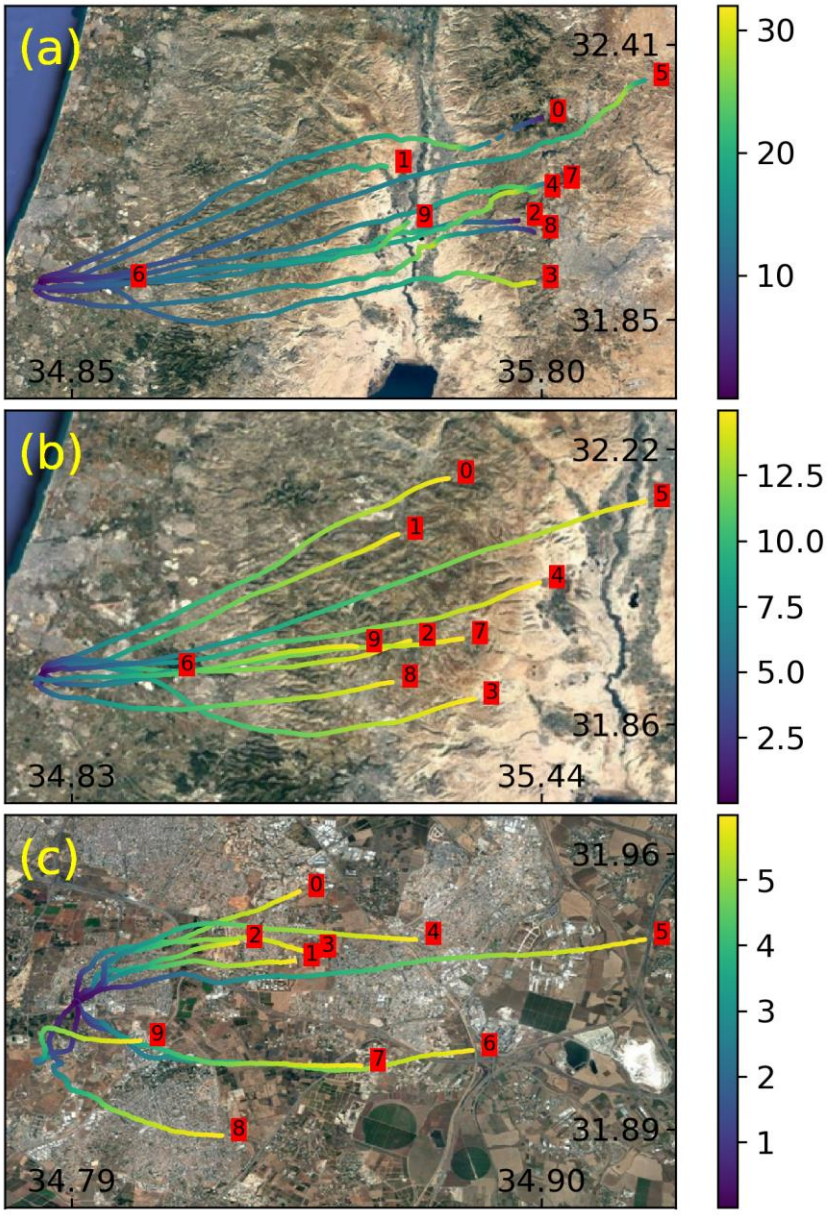

Figure 1. Flight paths of the radiosondes sketched over a space of geographical coordinates of longitude and latitude with a satellite base image. The different trajectories are labeled by numbers in accordance with **Table 1**. The color of the line describing a trajectory varies according to the height of the radiosonde at the same location and is explained by the color bars on the right sides of the sub-panels (in km). (a) The radiosondes' full flight paths. The radiosondes start by flying in different directions up to a height of ~10 km, after which they all fly north-east. After reaching a maximum altitude of about 30 km, the radiosondes descend until landing, where their path ends. (b) The radiosondes' flight paths up to the ceilometer's maximum sensing altitude (~15 km). (c) The radiosondes' flight paths bounded to the same geographical area as the starting point.

Table 1. Timings and paths of the radiosondes. 10 radiosondes were floated during a week at various hours. The radiosondes reached a maximum height of about 30 km after about an hour and a half, and then landed back in about 20 minutes (from the radiosondes that transmitted until reaching back to the ground). Other than radiosonde number 6 which only reached heights of less than 8 km, the rest of the radiosondes provided data on heights beyond 20 km. The maximum flight distance from the initial point is 123 km

Radiosonde number	Floating time	Time until maximum height (hours)	Total broadcast time (hours)	Maximum horizontal distance (km)
0	26/11/2017 1 PM	1.71	1.97	102
1	26/11/2017 7 PM	1.27	1.27	71
2	27/11/2017 1 AM	1.12	1.45	92
3	27/11/2017 7 AM	1.52	1.53	94
4	27/11/2017 1 PM	1.45	1.45	96
5	29/11/2017 1 PM	1.49	1.57	123
6	29/11/2017 7 PM	0.44	0.44	15
7	30/11/2017 1 AM	1.57	1.68	100
8	30/11/2017 7 AM	1.53	1.86	94
9	30/11/2017 1 PM	1.57	1.6	71

3 Results and discussion

3.1 Radiosondes' flight paths and measured profiles

Figure 1 shows the radiosondes' flight paths. While at the beginning of their paths, the radiosondes fly in different horizontal directions, after reaching a height of about 10 km, all the radiosondes flew to the northeast. The radiosondes reached a maximum altitude of $\sim 30\ km$, which is almost twice the ceilometer's maximum measurement height. However, the measurements are not well localized and spread over horizontal distances of about 120 km. When limiting the results to the ceilometer's maximum altitude range of 15 km, the horizontal spread of the radiosondes flight paths is reduced to about 80 km, and when limiting the radiosondes measurement to the same geographical area as the starting point, a lowland area, then the radiosondes reach a maximum height of about 6 km, and the horizontal spread is only about 13 km.

Figure 2 shows the temperature and humidity data measured by each of the radiosondes. Although the data was measured at different times of day, similar features can be identified. The temperature decreases with altitude to a minimum of $-70(10)\ {}^{O}C$, located around an altitude of 16-17 km and from there increases with altitude, and the humidity curves behave erratically up to a certain altitude from which the humidity is stable and negligible.

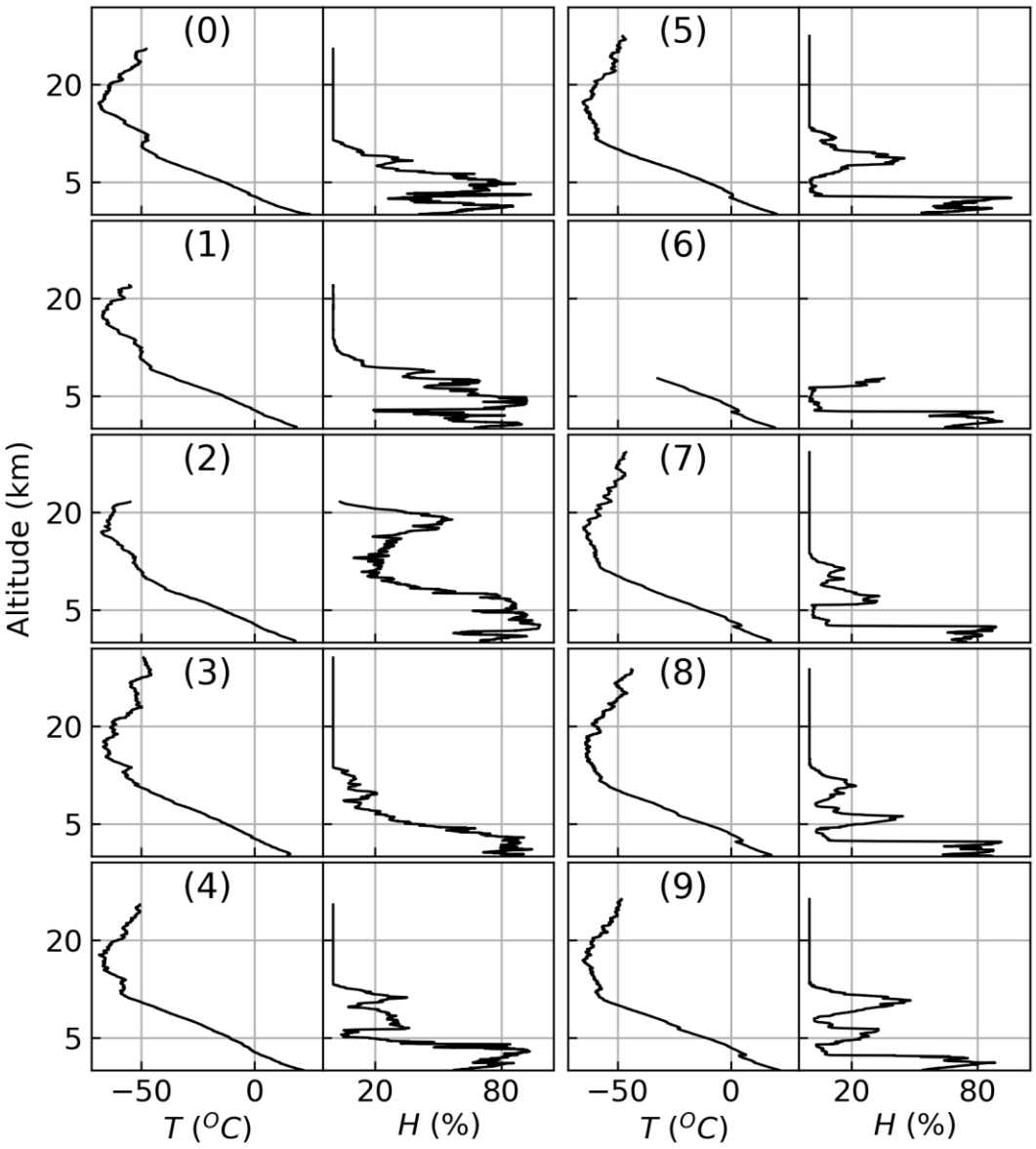

Figure 2. Temperature and humidity data measured by each of the radiosondes. The figure is divided into ten panels, each showing data from a single radiosonde, numbered according to the radiosondes numbers as in **Table 1**, and divided into two sub-panels for temperature and humidity measurements.

3.2 Time and height matching of the radiosonde and ceilometer measurements

The radiosonde gradually climbs the atmosphere, measuring a series of air parcels at different times, altitudes, and geographical location due to the existence of a finite horizontal wind. It reaches its maximum height after about an hour and a half, which is long enough for atmospheric variables and its location to change considerably, making the measurement unrepresentative. This is in contrast to the ceilometer's measurement which is acquired almost instantly. Therefore, in order to compare data from these two devices, an equivalent ceilometer optical backscatter profile was constructed according to each radiosonde flight.

Since the radiosondes all started ascending from roughly the same location where the ceilometer is and are affected from the same wind as the measured air, an air volume measured at a particular geographical point by a radiosonde may have been measured by the ceilometer at a different time. we may use the horizontal wind speed measurements and the ceilometer and radiosondes locations in order to retrace the moments when these air parcels were above the ceilometer. The distance between two locations on the earth's surface is calculated by using the Haversine formula.(Sinnott, 1984) The ceilometer's and radiosondes' locations are defined in terms of geographical coordinates as $\vec{r}^{ceil}$ and $\vec{r}^{sonde}(z)$ respectively, along with the following auxiliary function

$$f\left(\vec{r}^{sonde}, \vec{r}^{ceil}\right) = \sin^2\left(\frac{\Delta\vec{r}_y}{2}\right) + \cos\left(\vec{r}_y^{ceil}\right)\cos\left(\vec{r}_y^{sonde}\right)\sin^2\left(\frac{\Delta\vec{r}_x}{2}\right) \qquad (3)$$

where $\Delta\vec{r}(z) = \vec{r}^{sonde}(z) - \vec{r}^{ceil}$. Therefor the lateral distance between these two locations is

$$d(z) = 2R_e \tan^{-1}\left(\sqrt{\frac{f(\vec{r}^{sonde}(z), \vec{r}^{ceil})}{1 - f(\vec{r}^{sonde}(z), \vec{r}^{ceil})}}\right) \qquad (4)$$

The travel time will therefore be

$$\Delta t(z) = \frac{d(z)}{V_{Hor}(z)} \qquad (5)$$

where $V_{Hor}(z)$ is the horizontal wind velocity measured by the radiosonde at height z, and R_e is Earth's mean radius. For each radiosonde measurement altitude, z_n, the data for ranges between $B((z_{n-1} + z_n)/2)$ and $B((z_n + z_{n+1})/2)$ from the ceilometer measurement temporally closest to the moment where the air parcel was above it was concatenated to the data corresponding to previous altitudes until the maximum jointly available height was reached.

Figure 3 shows the radiosondes' temperature and humidity measurements and the temporally matched ceilometer's measurements (B). The measurements' altitude range is the same as the ceilometer's maximum range, ~15 km, which means that the radiosonde data was collected across ~80 km of lateral distance which may complicates this comparison due to uneven conditions and nonlinear trajectories. However, two considerations may resolve this complication: 1) While the optical backscatter data shows very sharp and high peaks which probably originates from the existence of clouds, its signal-to-noise ratio is quite low for heights above 3 km for many backscatter profiles. 2) Beyond the general trends in temperature and humidity seen in **Figure 2**, one can spot more subtle changes in temperature that in some panels manifest as local minimum

and maximum values accompanied by sharp changes in humidity (marked by red arrows. In other panels it is less obvious). These are identified as inversion layers and occur at heights up to ~3 km as well. Considering the altitudes of these inversions reinforced by existing knowledge on the structure of the ABL (Lee et al., 2019; Stull, 1988a) together with the altitude dependence of the signal to noise ratio, it is apparent that the most meaningful altitude range for a comparative analysis of data from radiosondes and ceilometer is below 3 km. This means that the flight paths to be considered shouldn't extend beyond those depicted in **Figure 1** c, which are all contained

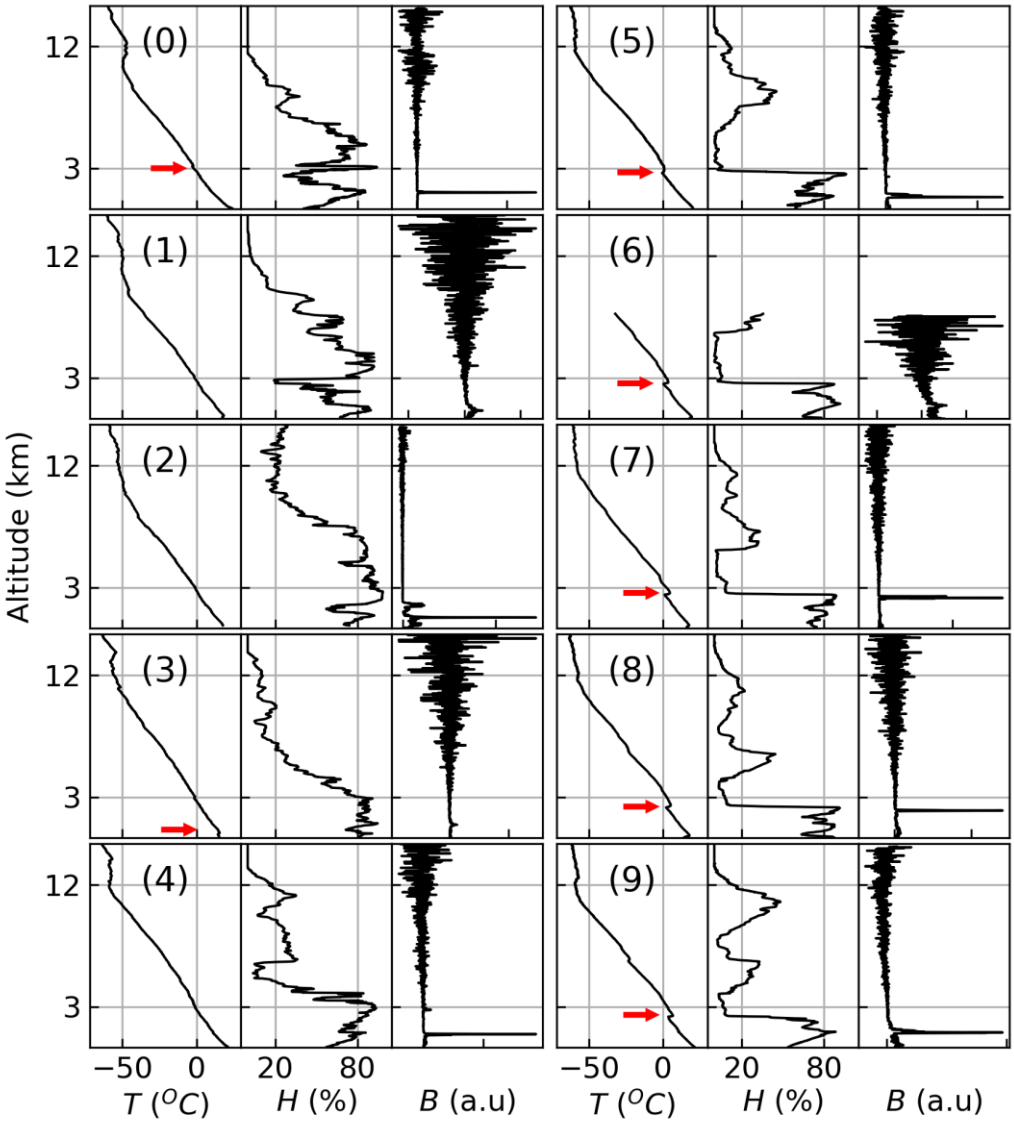

Figure 3. Temperature and humidity data measured by each of the radiosondes vs. the temporally matched ceilometer measurements. The altitude range is set according to the ceilometer's maximum range, ~15 km. The figure is divided into ten panels, each showing data from a single radiosonde, numbered according to the radiosondes numbers as in **Table 1**, and divided into three sub-panels for temperature, humidity and optical back-scatter measurements.

within the same geographical area as the starting point, a lowland area, with topographical difference below 100 m.

3.3 Relating the ceilometer's signal to the scatterers' density

The ceilometer's radiation backscattering measurements are described by the definition of B and Eq. (2), where the volume extinction coefficient, $\alpha(z) = n_d(z)\sigma_\lambda$, depends on the density of the scatterers, n_d, and the radiation scattering cross-section area σ_λ. Assuming spherical scatterers with radius r_d, $\sigma_\lambda = Q_s \pi r_d^2$ is dependent on the geometrical cross section area and on the extinction efficiency, Q_s, which like n_d is dependent on r_d.

Figure 4 shows the dependencies of n_d and Q_s on r_d. Q_s (solid line) is calculated from Mie theory for $\lambda = 910\,nm$ and goes to zero for $r_d \to 0$, reaches a maximum value of 4 for $r_d = \lambda$, and converges to 2 for $r_d \gg \lambda$.(Bohren & Huffman, 1983b) Normalized n_d (dashed line) is calculated according to Eq. (1) with $\bar{r}_d = 3.5\,\mu m$ and $\sigma_d = 0.35\,\mu m$ which should fit the particle size distribution in a cumulus cloud which is expected to be the main scatterer, due to the season, lack of precipitations, visual observation, and altitude range.(Goldreich, 2003a, 2003b; "Israel Meteorological Service," n.d.; Measures, 1992; Takeuchi, 2005)

Since the cilometer's wavelength is smaller than this cloud size distribution's typical particle, and under the approximation of mono-dispersity, the cross-section can be set as a constant, $\sigma_\lambda = 2\pi\bar{r}_d^2$.

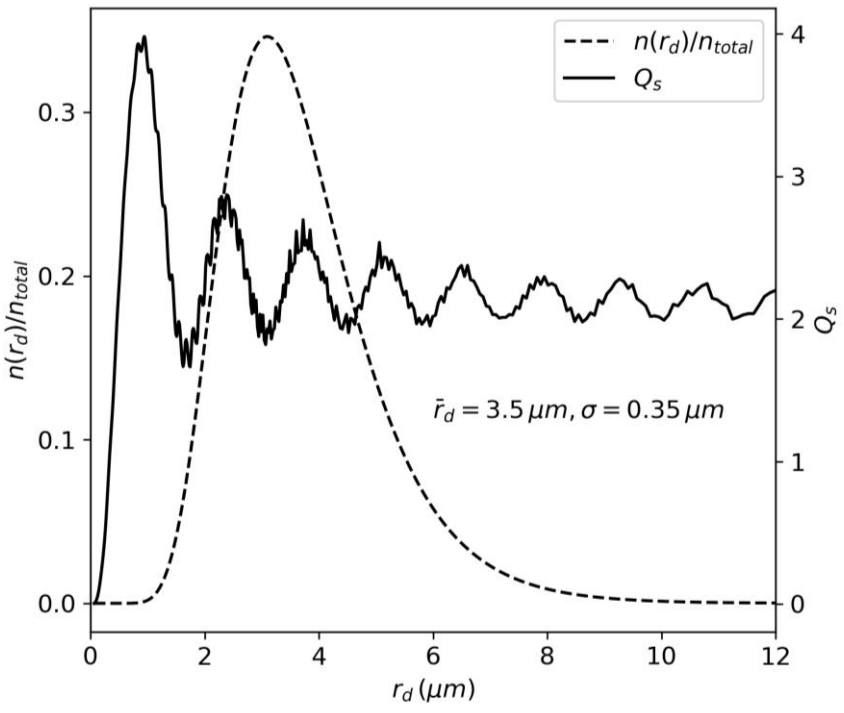

Figure 4. Normalized distribution of cloud droplet sizes, $n(r_d)/n_{total}$, (dashed line) and dependence of radiation extinction efficiency, Q_s, at wavelength of $\lambda = 910\,nm$ (continuous line) in droplet size, r_d. The droplet sizes are log-normal distributed, with the distribution's median at 3.5 μm and its width is 0.35 μm.

For the same reason, $S(z)$ is also a constant (back-scattering from particles identical in size and composition), and $B(z)$ can be written as

$$B(z) \cong An_d(z)e^{-2\sigma_\lambda \int_0^z n_d(z')dz'} \quad (6)$$

where A is a proportionality constant. Thus, with Eq. (6), it is possible by having a measure of B to have a measure of n_d, or more precisely for this work, quantify the mechanism that is responsible for n_d.

3.3.1 Formation of scatterers in the atmosphere

The ceilometer's measurement is only sensitive to the existence of particles with diameters equal or larger than the ceilometer's wavelength, but the ability of these large particles to reach a certain height decreases with height (Kleinman & Daum, 1991), so due to the absence of molecules other than water that can undergo a phase transition in the discussed heights (Wallace & Hobbs, 2006a, 2006b), the existence of these particles at these heights will result from water adsorption on smaller particles and coalescence of water covered particles,(Jonas & Mason, 1974; Kovetz & Olund, 1969) forming a droplet population with n_d density. Since most aerosol particles in the atmosphere over Israel originate from the nearby large desert area and, unless went several stages of atmospheric processing, have poor water adsorption capabilities, (Attwood & Greenslade, 2011; Chester, 1990; Cuadros et al., 2015; Falkovich et al., 2001; Ganor, 1975, 1991; Ganor & Foner, 1996; Ganor & Mamane, 1982; Levi & Rosenfeld, 1996; Levin et al., 1990; Wurzler et al., 2000) for a process of water adsorption on these particles to still occur, the water molecules should form a shell around a particle that will hold itself intact with the help of the water molecules' strong hydrogen bonds. This phenomenon is known as a hydrophobic force. It acts when introducing a non-polar solute into water and is caused by the entropy loss minimization to the network of water molecules.(Schauperl et al., 2016; Silverstein, 1998; Voet & Voet, 2011) The probability for this process is dependent on the density of gaseous water molecules, n_v, which we calculate from the partial pressure of the water vapor in the atmosphere, P_v, and the temperature, T, by using the ideal gas law

$$n_v = \frac{P_v}{k_B T} \quad (7)$$

where k_B is the Boltzmann constant. The partial pressure of the water vapor in the atmosphere is calculated with (Ahrens & Henson, 2019a)

$$P_v = \phi P^*_{H_2O} \quad (8)$$

where ϕ is the relative humidity measured by the radiosonde, and $P^*_{H_2O}$ is the water's vapor pressure calculated according to the Buck equation (Buck, 1981; Buck Research Instruments, 2012)

$$P^*_{H_2O}(T) = a \exp\left[\left(b - \frac{T}{d}\right)\left(\frac{T}{c+T}\right)\right] \quad (9)$$

where $a = 6.1121\ mbar$, $b = 18.678$, $c = 257.14\ ^oC$, $d = 234.5\ ^oC$, and T is in degrees Celsius.

Water molecules move through space and scatter off other particles as long as they continue failing to adhere to these particles. As stated above, the water molecules will permanently adhere to a particle if there are enough molecules to form a shell around it, but this has to occur faster than the collision (reorganization) time of the water molecules, t_c, and if it succeeds the particle could grow to a size measurable by the ceilometer by adsorbing more water vapor or coalescing with other droplets. In a particle system subjected to certain pressure and temperature conditions, t_c can be calculated by again using the ideal gas law together with the known relations $\frac{3}{2}k_BT = \frac{1}{2}mv^2$, $v = l_c/t_c$, $l_c\sigma = 1/n$, $\sigma = \pi r_p^2$, where v is the particles' velocity, n is the particles' density, m is the particles' mass, l_c is the typical distance between the particles, σ is the particles' scattering cross section area, and r_p is the particles radius, in order to obtain

$$t_c = \sqrt{\frac{mk_BT}{3P^2\left(\pi r_p^2\right)^2}} \tag{10}$$

For water molecules ($m = m_{H_2O} \cong 18\ amu, 2r_p = 2r_{H_2O} = 2.74$ Å) at room temperature and atmospheric pressure $t_c \cong 1\ nsec$.(D'Arrigo, 1978; Zhang & Xu, 1995)

At the dew temperature, T_{dew}, there is an equilibrium between the gaseous and the liquid phase. There will be enough thermal energy to transform from liquid (adsorbed) to gaseous phase only if the excess energy above the thermal energy of the dew temperature is greater than the latent heat energy per particle (the enthalpy), E_{cond}, which is

$$E_{cond}(T) = L_W(T)\rho_M/N_A \tag{11}$$

where ρ_M is the molar mass of water, N_A is the Avogadro number, and L_W is the latent heat energy of water, empirically determined as (R. R. Rogers & Yau, 1989)

$$L_W(T) = (2500.8 - 2.36T + 0.0016T^2 - 0.00006T^3)\ J/g \tag{12}$$

The dew temperature is calculated with the Magnus equation (Magnus, 1844) which describes the relation between the temperature, the relative humidity, and the water vapor's partial pressure, in its reciprocal form

$$T_{dew} = \frac{c\gamma_m(T,\phi)}{b - \gamma_m(T,\phi)} \tag{13}$$

where $\gamma_m(T,\phi) = \ln\left(\phi P^*_{H_2O}(T)/a\right)$, and all other constants are the same as in equation (9).

Therefore, considering the Boltzmann factor for this process, for $T \geq T_{dew}$, a water molecule condensation probability is

$$P_{cond} = e^{\frac{k_B(T_{dew}-T)}{E_{cond}}} \tag{14}$$

Since the sizes of the CCNs are later estimated to be as small as 50 nm, Köhler theory is taken into consideration,(Köhler, 1936; Seinfeld & Pandis, 2016a) but since the CCNs are assumed to be non-soluble,(Attwood & Greenslade, 2011; Falkovich et al., 2001; Ganor, 1991) Only the curvature is to have some effect due to surface tension (Berry, 1971). According to the Kelvin

equation,(Seinfeld & Pandis, 2016b) the change to the condensation probability is thus estimated to be $\Delta P_{cond}/P_{cond} < 0.007\%$.

As stated above, in order for the aerosol particles to act as efficient condensation nuclei, an initial water molecules shell (consisting of η molecules) should be created around it in a time shorter than t_c, a process whose probability is P_{cond}^{η}. Considering an abundant source of CCNs of finite sizes (the smallest of which can be fully covered by N_{mol} molecules), the total probability for this process is (assuming $k_B|T_{dew} - T|/E_{cond} \ll 1$)

$$P_T = \sum_{\eta=N_{mol}}^{\infty} P_{cond}^{\eta} = \frac{-E_{cond}}{k_B(T_{dew} - T)} e^{N_{mol}\frac{k_B(T_{dew}-T)}{E_{cond}}} \quad (15)$$

Therefore, the drop density is

$$n_d = n_v P_T \quad (16)$$

3.3.2 Fitting the radiosonde data transformation to the ceilometer's measurements

Using the above relations, the radiosondes measurements were transformed into simulated optical back-scattered curves and fitted to the ceilometer's measurement by adjusting N_{mol}. **Figure 5** shows a comparison of n_d calculated using Equation (16), B' calculated using Equation (6), and B measured by the ceilometer and temporally adjusted for the radiosonde measurements as explained above. There seems to be a high visual correlation between B and B', which is mostly well confirmed by calculated correlation values, $\rho_{B,B'}$, between the two (**Table 2**). This confirms the physical basis for the model presented here. The model also allows us to estimate the minimum condensation nuclei size of the droplets from N_{mol} by considering the effective coverage area of "spherical" water molecules on spherical condensation nuclei

$$r_{nuc} = \left(\frac{N_{mol}\pi r_{H_2O}^2}{4\pi f_{pack}}\right)^{1/2} = \sqrt{\frac{N_{mol}}{4f_{pack}}} r_{H_2O} \quad (17)$$

where r_{H_2O} is the water molecule radius and $f_{pack} \cong 0.9069$ is the molecules' packing ratio on top of the particle's surface.(Conway & Sloane, 1999) Values for r_{nuc} from these comparisons are shown in **Table 2**, and have a mean value of $2r_{nuc} = 46.7(18)\, nm$. This size does indeed correspond to the known minimum size of cloud condensation nuclei.(Mahowald et al., 2014)

Furthermore, although one would expect the ceilometer's signal to always correspond to the water droplet density, it often displays a strong signal where the density is relatively low, and a weak signal where the density is high. This, of course, is due to the exponent term in Equation (2) which more strongly attenuates the signal for greater distances.

While it seems that this model successfully describes most of the ceilometer's measurements features, some measurements contain a feature that is not described by the model, and therefore their quality of fitting is lower (for example – panel 1 in Figure 5). This feature is pronounced in measurements with relatively low signal to noise ratios and is located at heights of below 1 km. The feature is shaped like an asymmetrical bell curve centered around 0.5 km, which can correspond to finite wavelength-sized aerosol concentrations expected at low altitudes,(Kleinman

Table 2. Correlation values, $\rho_{B,B'}$, and condensation nuclei diameters, $2r_{nuc}$, calculated for each of the radiosondes. $\rho_{B,B'}$ values are usually high, except for measurements where the signal to noise ratio is low, and their average value is $0.85(5)$. $2r_{nuc}$ values are narrowly distributed around an average value of $46.7(18)$ nm corresponding to the known minimum size of cloud condensation nuclei.

Radiosonde number	$\rho_{B,B'}$	$2r_{nuc}$
0	0.99	44.1
1	0.65	48.8
2	0.75	42.4
3	0.81	56.6
4	0.97	37.5
5	0.92	43.9
6	0.52	47.7
7	0.99	51.9
8	0.97	51.1
9	0.90	43.2

& Daum, 1991) together with non-constant LiDAR overlap function (Equation (2)). Another explanation for these anomalies could be scattered LASER radiation contribution of second or higher order that is becoming significant for sensing ranges that are equal or smaller than the visibility distance or than the source-detector distance of the ceilometer.(Ding et al., 2010) The in-depth study of these anomalies will be done in a future work.

4 Conclusions

In this work, a comparative analysis of ceilometer and radiosonde measurements was carried out using a set of measurements from both systems collected simultaneously over a week at the end of November. A method for temporarily adjusting the measurement systems data was applied by weighting the instantaneous locations of the radiosondes and wind speeds at these locations.

A transformation has been proposed for turning the radiosonde signals into simulated optical back-scatter signal that would best fit the ceilometer's signal by linking the two signal types with the density of optical scattering elements in the atmosphere. This transformation allowed examining the condensation processes in the atmosphere that help to create these scatterers, and identify the controlling factor in creating them and quantify it by fitting the transformed radiosonde data to the ceilometer's measurements. This provided a good match between the ceilometer's signal and the optical back-scatter simulated curves. In several measurements the heights of the sharp peaks in the ceilometer's signal do not correspond with the heights of the highest water droplet density, due to finite drop density values that are amplified due to the exponent term in the LiDAR equation.

Acknowledgments, Samples, and Data

The authors declare no financial conflicts of interests. The data supporting the conclusions of this work can be obtained at the Mendeley Data server (Arielly, 2020).

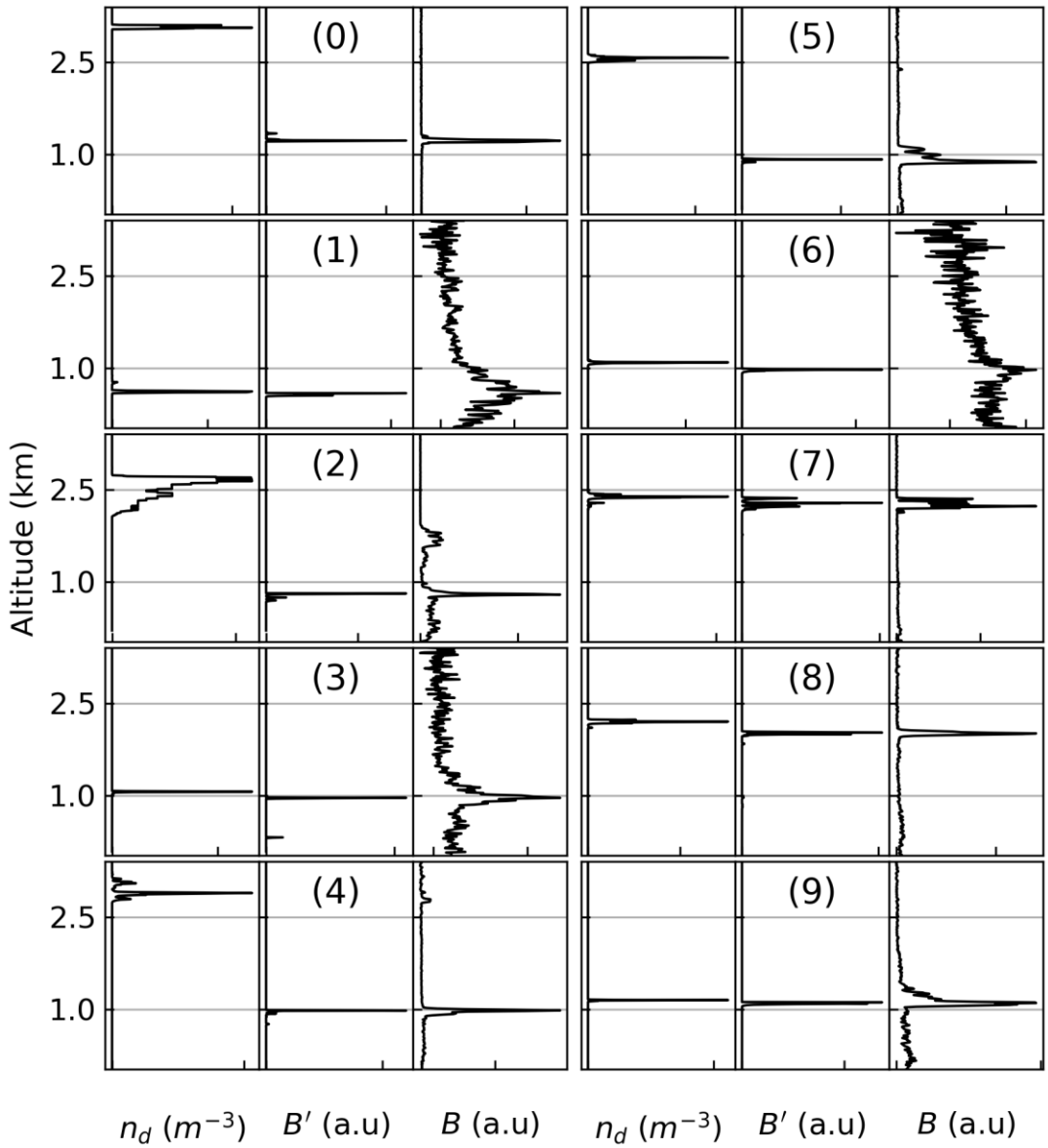

Figure 5. Comparison between the calculated drop densities, n_d, simulated ceilometer profiles, B', and measured ceilometer profiles, B. The altitude range was set to 3.4 km according to the identified inversion altitudes and to the signal to noise ratio (see text). The figure is divided into ten panels, each showing data corresponding to a single radiosonde, numbered according to the radiosondes numbers as in **Table 1**, and divided into three sub-panels for n_d, B' and B. There is usually a good fit between B' and B, so that even small features are successfully reproduced, such as secondary peaks near strong peaks in the signal. Correlation based fit values are shown in **Table 2**. When the signal-to-noise ratio is low, there is a significant contribution at low altitudes that is not reproduced by the model and has several explanations (see text). In four measurements (40%) the sharp peaks' altitudes in the ceilometer signal do not correspond to the altitudes where the droplet density is highest, due to finite droplet density values which are relatively amplified due to the exponent term in the LiDAR equation.

Ahrens, C. D., & Henson, R. (2019a). Humidity. In *Meteorology Today: An Introduction to Weather, Climate, and the Environment* (12th ed., pp. 95–107). Boston, MA, USA: Cengage Learning.

Ahrens, C. D., & Henson, R. (2019b). Radiation: Absorption, Emission, and Equilibrium. In *Meteorology Today: An Introduction to Weather, Climate, and the Environment* (12th ed., pp. 41–51). Boston, MA, USA: Cengage Learning.

Andreae, M. O., Charlson, R. J., Bruynseels, F., Storms, H., Grieken, R. V., & Maenhaut, W. (1986). Internal Mixture of Sea Salt, Silicates, and Excess Sulfate in Marine Aerosols. *Science*, *232*(4758), 1620–1623. https://doi.org/10.1126/science.232.4758.1620

Arielly, R. (2020). Ceilometer and Radiosonde Data - November 2017. *Mendeley Data*, *V1*. https://doi.org/10.17632/xrpshxvt8w.1

Attwood, A. R., & Greenslade, M. E. (2011). Optical Properties and Associated Hygroscopicity of Clay Aerosols. *Aerosol Science and Technology*, *45*(11), 1350–1359. https://doi.org/10.1080/02786826.2011.594462

Banakh, V. A., Smalikho, I. N., Köpp, F., & Werner, C. (1995). Representativeness of wind measurements with a cw Doppler lidar in the atmospheric boundary layer. *Applied Optics*, *34*, 2055–2067.

Banakh, V. A., Smalikho, I. N., Pichugina, E. L., & Brewer, W. A. (2010). Representativeness of measurements of the dissipation rate of turbulence energy by scanning Doppler lidar. *Atmos Ocean Opt*, *23*, 48–54.

Berry, M. V. (1971). The molecular mechanism of surface tension. *Physics Education*, *6*(2), 79–84. https://doi.org/10.1088/0031-9120/6/2/001

Bohren, C. F., & Huffman, D. R. (1983a). Absorption and Scattering by a Sphere. In *Absorption and Scattering of Light by Small Particles* (pp. 82–129). New York: John Wiley & Sons, Inc.

Bohren, C. F., & Huffman, D. R. (1983b). The Extinction Paradox; Scalar Diffraction Theory. In *Absorption and Scattering of Light by Small Particles* (pp. 107–111). New York: John Wiley & Sons, Inc.

Brümmer, B., Lange, I., & Konow, H. (2012). Atmospheric boundary layer measurements at the 280 m high Hamburg weather mast 1995-2011: mean annual and diurnal cycles. *Meteorologische Zeitschrift*, *21*(4), 319–335. https://doi.org/10.1127/0941-2948/2012/0338

Buck, A. L. (1981). New equations for computing vapor pressure and enhancement factor. *Journal of Applied Meteorology*, *20*, 1527–1532.

Buck Research Instruments, L. (2012). Model CR-1A Hygrometer With Autofill Operating Manual. Boulder, Colorado.

Cess, R. D., Zhang, M., Wielicki, B. A., Young, D. F., Zhou, X.-L., & Nikitenko, Y. (2001). The Influence of the 1998 El Niño upon Cloud-Radiative Forcing over the Pacific Warm Pool. *Journal of Climate*, *14*(9), 2129–2137. https://doi.org/10.1175/1520-0442(2001)014<2129:TIOTEN>2.0.CO;2

Chester, R. (1990). The atmospheric transport of clay minerals to the world ocean. *Sciences Géologiques, Bulletins et Mémoires*, *88*(1), 23–32.

Conway, J. H., & Sloane, N. J. A. (1999). The Sphere Packing Problem. In M. Berger, J. Coates, & S. R. S. Varadhan (Eds.), *Sphere Packings, Lattices and Groups* (3rd ed., pp. 1–21). New York: Springer.

Cuadros, J., Diaz-Hernandez, J. L., Sanchez-Navas, A., & Garcia-Casco, A. (2015). Role of clay minerals in the formation of atmospheric aggregates of Saharan dust. *Atmospheric Environment*, *120*, 160–172. https://doi.org/10.1016/j.atmosenv.2015.08.077

D'Arrigo, J. S. (1978). Screening of membrane surface charges by divalent cations: an atomic representation. *American Journal of Physiology-Cell Physiology*, *235*(3), C109–C117. https://doi.org/10.1152/ajpcell.1978.235.3.C109

Ding, H., Xu, Z., & Sadler, B. M. (2010). A Path Loss Model for Non-Line-of-Sight Ultraviolet Multiple Scattering Channels. *EURASIP Journal on Wireless Communications and Networking*, *2010*(1), 598572. https://doi.org/10.1155/2010/598572

Eckstein, J., Ruhnke, R., Zahn, A., Neumaier, M., Kirner, O., & Braesicke, P. (2017). An assessment of the climatological representativeness of IAGOS-CARIBIC trace gas measurements using EMAC model simulations. *Atmos. Chem. Phys.*, *17*, 2775–2794.

Falkovich, A. H., Ganor, E., Levin, Z., Formenti, P., & Rudich, Y. (2001). Chemical and mineralogical analysis of individual mineral dust particles. *Journal of Geophysical Research: Atmospheres*, *106*(D16), 18029–18036. https://doi.org/10.1029/2000JD900430

Gagin, A. (1965). Ice nuclei,their physical characteristics and possible effect on precipitation initiation. In *Proceedings of the International Conference on Cloud Physics* (pp. 155–162). Tokyo and Sapporo.

Ganor, E. (1975). *Atmospheric Dust in Israel — Sedimentological and Meteorological Analysis of Dust Deposition* (Phd). Hebrew University, Jerusalem, Israel.

Ganor, E. (1991). The composition of clay minerals transported to Israel as indicators of Saharan dust emission. *Atmospheric Environment. Part A. General Topics*, *25*(12), 2657–2664. https://doi.org/10.1016/0960-1686(91)90195-D

Ganor, E., & Foner, H. A. (1996). The Mineralogical and Chemical Properties and the Behaviour of Aeolian Saharan Dust Over Israel. In S. Guerzoni & R. Chester (Eds.), *The Impact of Desert Dust Across the Mediterranean* (pp. 163–172). Dordrecht: Springer Netherlands. https://doi.org/10.1007/978-94-017-3354-0_15

Ganor, E., & Mamane, Y. (1982). Transport of Saharan dust across the eastern Mediterranean. *Atmospheric Environment (1967)*, *16*(3), 581–587. https://doi.org/10.1016/0004-6981(82)90167-6

Ghadiri, M., Chrzanowski, W., & Rohanizadeh, R. (2015). Biomedical applications of cationic clay minerals. *RSC Advances*, *5*(37), 29467–29481. https://doi.org/10.1039/C4RA16945J

Golbon-Haghighi, M.-H., Zhang, G., Li, Y., & Doviak, J. R. (2016). Detection of Ground Clutter from Weather Radar Using a Dual-Polarization and Dual-Scan Method. *Atmosphere* . https://doi.org/10.3390/atmos7060083

Goldreich, Y. (2003a). Precipitation. In *The Climate Of Israel - Observations, Research and Application* (1st ed., pp. 55–91). New York: Springer.

Goldreich, Y. (2003b). Spatial Cloudiness And Temporal Distribution. In *The Climate Of Israel - Observations, Research and Application* (1st ed., pp. 127–129). New York: Springer.

Haszpra, L. (1999). On the representativeness of carbon dioxide measurements. *Journal of Geophysical Research: Atmospheres*, *104*, 26953–26960.

Henne, S., Brunner, D., Folini, D., Solberg, S., Klausen, J., & Buchmann, B. (2010). Assessment of parameters describing representativeness of air quality in-situ measurement sites. *Atmospheric Chemistry and Physics*, *10*, 3561–3581.

Israel Meteorological Service. (n.d.). Retrieved July 10, 2020, from https://ims.data.gov.il/

Jenkin, M. E., & Clemitshaw, K. C. (2000). Ozone and other secondary photochemical pollutants: chemical processes governing their formation in the planetary boundary layer. *Atmospheric Environment*, *34*(16), 2499–2527. https://doi.org/10.1016/S1352-2310(99)00478-1

Jonas, P. R., & Mason, B. J. (1974). The evolution of droplet spectra by condensation and coalescence in cumulus clouds. *Quarterly Journal of the Royal Meteorological Society*, *100*(425), 286–295. https://doi.org/10.1002/qj.49710042503

Kitchen, M. (1989). Representativeness errors for radiosonde observations. *Q.J.R. Meteorol. Soc.*, *115*, 673–700.

Kleinman, L. I., & Daum, P. H. (1991). Vertical distribution of aerosol particles, water vapor, and insoluble trace gases in convectively mixed air. *Journal of Geophysical Research: Atmospheres*, *96*(D1), 991–1005. https://doi.org/10.1029/90JD02117

Köhler, H. (1936). The nucleus in and the growth of hygroscopic droplets. *Transactions of the Faraday Society*, *32*(0), 1152–1161. https://doi.org/10.1039/TF9363201152

Koren, I., Kaufman, Y. J., Remer, L. A., & Martins, J. V. (2004). Measurement of the Effect of Amazon Smoke on Inhibition of Cloud Formation. *Science*, *303*(5662), 1342–1345. https://doi.org/10.1126/science.1089424

Kovetz, A., & Olund, B. (1969). The Effect of Coalescence and Condensation on Rain Formation in a Cloud of Finite Vertical Extent. *Journal of the Atmospheric Sciences*, *26*(5), 1060–1065. https://doi.org/10.1175/1520-0469(1969)026<1060:TEOCAC>2.0.CO;2

Lee, J., Hong, J. W., Lee, K., Hong, J., Velasco, E., Lim, Y. J., et al. (2019). Ceilometer Monitoring of Boundary-Layer Height and Its Application in Evaluating the Dilution Effect on Air Pollution. *Boundary-Layer Meteorology*. https://doi.org/10.1007/s10546-019-00452-5

Levi, Y., & Rosenfeld, D. (1996). Ice Nuclei, Rainwater Chemical Composition, and Static Cloud Seeding Effects in Israel. *Journal of Applied Meteorology (1988-2005)*, *35*(9), 1494–1501.

Levin, Z., Price, C., & Ganor, E. (1990). The contribution of sulfate and desert aerosols to the acidification of clouds and rain in Israel. *Atmospheric Environment. Part A. General Topics*, *24*(5), 1143–1151. https://doi.org/10.1016/0960-1686(90)90079-3

Levin, Z., Ganor, E., & Gladstein, V. (1996). The Effects of Desert Particles Coated with Sulfate on Rain Formation in the Eastern Mediterranean. *Journal of Applied Meteorology*, *35*(9), 1511–1523. https://doi.org/10.1175/1520-0450(1996)035<1511:TEODPC>2.0.CO;2

Magnus, G. (1844). Versuche über die Spannkräfte des Wasserdampfs. *Annalen Der Physik*, *137*(2), 225–247. https://doi.org/10.1002/andp.18441370202

Mahowald, N., Albani, S., Kok, J. F., Engelstaeder, S., Scanza, R., Ward, D. S., & Flanner, M. G. (2014). The size distribution of desert dust aerosols and its impact on the Earth system. *Aeolian Research*, *15*, 53–71. https://doi.org/10.1016/j.aeolia.2013.09.002

Mattis, I., & Wagner, F. (2014). *E-PROFILE: Glossary of lidar and ceilometer variables*. Department of Research and Development, Meteorological Observatory

Hohenpeißenberg, German Weather Service (DWD), Hohenpeißenberg, Germany. Retrieved from http://eumetnet.eu/wp-content/uploads/2016/10/ALC_glossary.pdf

McGrath, R., Semmler, T., Sweeney, C., & Wang, S. (2006). Impact of Balloon Drift Errors in Radiosonde Data on Climate Statistics. *Journal of Climate*, *19*(14), 3430–3442. https://doi.org/10.1175/JCLI3804.1

Measures, R. M. (1992). Volume Scattering Coefficients and Phase Functions. In *Laser Remote Sensing: Fundamentals and Applications* (pp. 53–58). Malabar, Florida: Krieger publishing company.

Nappo, C. J., Caneill, J. Y., Furman, R. W., Gifford, F. A., Kaimal, J. C., Kramer, M. L., et al. (1982). The Workshop on the Representativeness of Meteorological Observations, June 1981, Boulder, Colo. *Bulletin of the American Meteorological Society*, *63*(7), 761–764.

Nolan, D. S., Zhang, J. A., & Stern, D. P. (2009). Evaluation of Planetary Boundary Layer Parameterizations in Tropical Cyclones by Comparison of In Situ Observations and High-Resolution Simulations of Hurricane Isabel (2003). Part I: Initialization, Maximum Winds, and the Outer-Core Boundary Layer. *Monthly Weather Review*, *137*(11), 3651–3674. https://doi.org/10.1175/2009MWR2785.1

Paluch, I. R., & Lenschow, D. H. (1991). Stratiform Cloud Formation in the Marine Boundary Layer. *Journal of the Atmospheric Sciences*, *48*(19), 2141–2158. https://doi.org/10.1175/1520-0469(1991)048<2141:SCFITM>2.0.CO;2

Piersanti, A., Vitali, L., Righini, G., Cremona, G., & Ciancarella, L. (2015). Spatial representativeness of air quality monitoring stations: A gridmodel based approach. *Atmospheric Pollution Research*, *6*, 953–960.

Quan, J., Gao, Y., Zhang, Q., Tie, X., Cao, J., Han, S., et al. (2013). Evolution of planetary boundary layer under different weather conditions, and its impact on aerosol concentrations. *Particuology*, *11*(1), 34–40. https://doi.org/10.1016/j.partic.2012.04.005

Rogers, A., Walls, E., Henson, W., & Manwell, J. (2007). Addressing Ground Clutter Corruption of Sodar Measurements. In *45th AIAA Aerospace Sciences Meeting and Exhibit*. American Institute of Aeronautics and Astronautics. https://doi.org/doi:10.2514/6.2007-1226

Rogers, R. R., & Yau, M. K. (1989). Clausius-Clapeyron equation. In D. Ter-Haar (Ed.), *A Short Course in Cloud Physics* (3rd ed., pp. 12–16). Burlington, Massachusetts: Butterworth-Heinemann.

Rosenfeld, D., & Farbstein, H. (1992). Possible Influence of Desert Dust on Seedability of Clouds in Israel. *Journal of Applied Meteorology*, *31*(7), 722–731. https://doi.org/10.1175/1520-0450(1992)031<0722:PIODDO>2.0.CO;2

Schauperl, M., Podewitz, M., Waldner, B. J., & Liedl, K. R. (2016). Enthalpic and Entropic Contributions to Hydrophobicity. *Journal of Chemical Theory and Computation*, *12*(9), 4600–4610. https://doi.org/10.1021/acs.jctc.6b00422

Schwarz, M., Folini, D., Hakuba, M. Z., & Wild, M. (2017). Spatial Representativeness of Surface-Measured Variations of Downward Solar Radiation. *Journal of Geophysical Research: Atmospheres, 122*, 13,319-13,337.

Seidel, D. J., Sun, B., Pettey, M., & Reale, A. (2011). Global radiosonde balloon drift statistics. *Journal of Geophysical Research: Atmospheres*, *116*(D7). https://doi.org/10.1029/2010JD014891

Seinfeld, J. H., & Pandis, S. N. (2016a). Equilibrium Of Water Droplets In The Atmosphere. In *Atmospheric chemistry and physics: from air pollution to climate change* (3rd ed., pp. 708–719). New Jersey: Wiley & Sons.

Seinfeld, J. H., & Pandis, S. N. (2016b). Equilibrium Vapor Pressure Over A Curved Surface: The Kelvin Effect. In *Atmospheric chemistry and physics: from air pollution to climate change* (3rd ed., pp. 419–423). New Jersey: Wiley & Sons.

Silverstein, T. P. (1998). The Real Reason Why Oil and Water Don't Mix. *Journal of Chemical Education*, *75*(1), 116. https://doi.org/10.1021/ed075p116

Sinnott, R. W. (1984). Virtues of the Haversine. *Sky and Telescope*, *68*(2), 159.

Stull, R. B. (1988a). Mean Boundary Layer Characteristics. In *An Introduction to Boundary Layer Meteorology* (1st ed., pp. 2–19). Dordrecht: Kluwer Academic Publishers.

Stull, R. B. (1988b). Taylor's Hypothesis. In *An Introduction to Boundary Layer Meteorology* (1st ed., pp. 5–7). Dordrecht: Kluwer Academic Publishers.

Takeuchi, N. (2005). Model of Aerosol Size Distribution. In T. Fujii & T. Fukuchi (Eds.), *Laser Remote Sensing* (1st ed., pp. 92–95). Boca Raton, Florida: CRC press.

Vaisala. (2017a). Data Messages. In *Vaisala Ceilometer CL51 User Guide* (pp. 60–77). Vantaa: Vaisala Oyj.

Vaisala. (2017b). Introduction to Vaisala Ceilometer CL51. In *Vaisala Ceilometer CL51 User Guide* (pp. 19–20). Vantaa: Vaisala Oyj.

Voet, D., & Voet, J. G. (2011). Protein Stability. In *Biochemistry* (4th ed., pp. 259–266). NJ: Wiley & Sons.

Wallace, J. M., & Hobbs, P. V. (2006a). Chemical Composition. In R. DMOWSKA, D. HARTMANN, & H. T. ROSSBY (Eds.), *Atmospheric Science - An Introductory Survey* (2nd ed., pp. 8–9). London: Academic Press.

Wallace, J. M., & Hobbs, P. V. (2006b). Composition of Tropospheric Air. In R. DMOWSKA, D. HARTMANN, & H. T. ROSSBY (Eds.), *Atmospheric Science - An Introductory Survey* (2nd ed., pp. 153–157). London: Academic Press.

Weitkamp, C. (2005). Lidar: Introduction. In T. Fujii & T. Fukuchi (Eds.), *Laser Remote Sensing* (1st ed., pp. 7–13). Boca Raton, Florida: CRC pres.

Wurzler, S., Reisin, T. G., & Levin, Z. (2000). Modification of mineral dust particles by cloud processing and subsequent effects on drop size distributions. *Journal of Geophysical Research: Atmospheres*, *105*(D4), 4501–4512. https://doi.org/10.1029/1999JD900980

Yaalon, D. H., & Ganor, E. (1973). The Influence Of Dust On Soils During The Quaternary. *Soil Science*, *116*(3), 146–155.

Zhang, Y., & Xu, Z. (1995). Atomic radii of noble gas elements in condensed phases. *American Mineralogist*, *80*(7–8), 670–675. https://doi.org/10.2138/am-1995-7-803

Zhong, S., & Doran, J. C. (1997). A Study of the Effects of Spatially Varying Fluxes on Cloud Formation and Boundary Layer Properties Using Data from the Southern Great Plains Cloud and Radiation Testbed. *Journal of Climate*, *10*(2), 327–341. https://doi.org/10.1175/1520-0442(1997)010<0327:ASOTEO>2.0.CO;2